Original Research Article

Stability of Cracked Functionally Graded Graphene-Reinforced Beams under Magnetic Field

ABSTRACT

This paper studies linear dynamic stability of cracked functionally graded (FG) graphene platelet (GPL)-reinforced composite laminated beams subjected to the combined action of magnetic field and a periodic axial force. GPL weight fraction follows a layer-wise variation across the beam thickness. Effective material properties are estimated by micromechanics models, and the bending stiffness of the cracked section is evaluated by a rotational spring model. The governing equation is derived by Ritz method and Lagrange equation within the framework of the first-order shear deformation theory. The linear principle unstable regions of the cracked beams are determined by Bolotin method. Numerical results show that magnetic field intensity, GPL distribution pattern, boundary condition, crack depth and location have significant influence on the linear dynamic stability behaviors of the cracked beams.

Keywords: Crack; Functionally graded materials; Graphene platelet; The first-order shear deformation theory; Dynamic stability

1. INTRODUCTION

Traditional composites are prone to stress concentration at the interface of different components because of the mismatch of physical properties, which often leads to the presence of delamination or cracks when the structure is subjected to large mechanical or temperature load. In the cutting-edge scientific and technological fields such as aviation, ships, engines and so on, materials are often required to work in extreme environments such as ultra-high pressure, ultra-high / low temperature, etc. [1]. Relying on traditional composites can no longer meet the strict requirements of structural performance in these fields. With the rapid development of material science, polymer nanocomposites, as the most promising direction of composites, now occupy an important position in the development strategy of new materials all over the world.

Adding a small amount of GPLs to the polymer matrix can significantly improve the mechanical, thermal and electrical properties of the composites [2-4]. Compared with carbon nanotubes, GPLs have better reinforcement properties for matrix mechanical parameters [2]. The reasonable functional gradient distribution of multiphase materials can reduce or even eliminate the interface damage caused by different properties of different materials. Recently, Yang's group [5-7] introduced the concept of FG multilayer materials into GPL-reinforced composites. Through systematic research, it is found that the reasonable distribution of graphene in the matrix can further increase the natural frequencies and static critical buckling loads and reduce the forced vibration response of the structures. Kitipornchai et al. [8] studied the buckling behavior of FG GPL-reinforced composite (FG-GPLRC) porous beams. The results show that the critical buckling loads of porous beams can be effectively increased when both GPL dispersion and porosity distribution pattern are non-uniform and symmetric. Li et al. [9] studied the static buckling of FG-GPLRC porous plates based on an isogeomertic analysis. Lei et al. [10] investigated the buckling behavior of FG-GPLRC laminated plates in thermal environment based on the meshless kp-Ritz method.

Different from static buckling, instability can occur when a structure is subjected to a dynamic load with a small amplitude [11]. Therefore, dynamic stability analysis has been attracted many attentions in recent years to keep structures safe and serviceable during the entire lifetime. Wu et al. [12] used Timoshenko beam theory and Bolotin method to determine the dynamic instability regions of FG-GPLRC beams by considering temperature effects. It was found that distributing more GPLs near the surfaces can greatly improve the dynamic stability of the beams. In addition, Zhao et al. [13] analyzed the dynamic instability of FG-GPLRC porous arches with fixed ends by using the classical Euler-Bernoulli beam theory. The results show that the arch with GPL reinforcement and symmetrical and uneven distribution of porosity has remarkable dynamic stability. Yang et al. [14] also studied the dynamic buckling of FG-GPLRC shallow arches

under central step load. With the development of science and technology, electromagnetic structures are common in high-tech devices, such as micro / nano devices, high-speed maglev trains and so on. The electromagnetic environment can affect the reliability and safety of elastomer operation. GPL-reinforced composites have a wide range of engineering applications because of their excellent mechanical properties, and the analysis of the structural behaviors under magnetic field is an unavoidable topic. Sobhy [15] analyzed the buckling and vibration of FG-GPLRC aluminum sandwich curved beams exposed to a magnetic field. Zhang et al. [16] studied the natural frequencies and static buckling of FG-GPLRC cylindrical shells under axial magnetic field, and found that the magnetic field has a significant effect on the structural behaviors of FG-GPLRC cylindrical shells.

The above studies shows that when the structure is subjected to time-varying axial load, dynamic instability caused by parametric resonance may occur. The mechanical properties of solid structures can be improved when they are subjected to magnetic fields. However, the above studies on FG-GPLRC structures are based on the ideal case without cracks. However, cracks can reduce the stiffness and strength and significantly affect the stability of the structures [17]. In this case, it is necessary to accurately determine the dynamic stability region, to better understand effects of parameters on the dynamic performance of cracked structures from the perspective of structural design. At present, the coupling effect of magnetic field and cracks on the dynamic stability behaviors of FG-GPLRC structures has not been reported yet.

In this paper, the linear dynamic stability of cracked FG-GPLRC beams under the combined action of magnetic field and periodic axial force is studied for the first time. Based on the first-order shear deformation beam theory, the energy function of cracked beam is established. The governing equation is derived by Ritz method and Lagrange equation, and the principle unstable region of the beam is determined by Bolotin method. The numerical simulation is performed to examine the effects of several parameters, such as magnetic field intensity, GPL distribution pattern, crack depth and location, on the linear principle unstable regions.

2. PROBLEM FORMULATION

Fig. 1(a) is a schematic diagram of a cracked FG-GPLRC laminated beam with N_L perfectly bonded layers. GPLs are randomly and uniformly dispersed in each layer, so they can be treated as isotropic uniform materials with layer-wise GPL concentrations. According to the distribution pattern of GPLs in the beam, the three cases (UD, FG-O and FG-X) shown in Fig. 1(b) are considered in this paper. GPL volume fraction in each layer is found in Ref. [12], that is, GPLs are concentrated near the neutral layer of FG-O beam and near the upper and lower surfaces of FG-X beam, but uniformly distributed in UD beam.

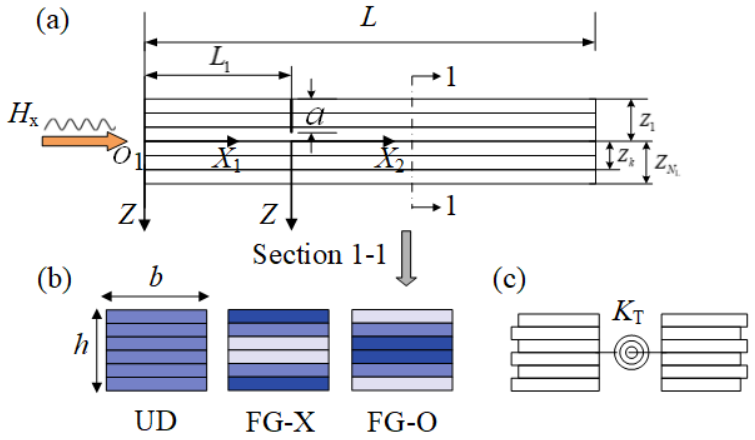

Fig.1 (a) Schematic diagram of cracked FG-GPLRC beam; (b) specific patterns of UD, FG-X and FG-O distribution; (c) rotational spring model

The modified Halpin-Tsai model and mixing rule [5] are used to estimate the effective Young's modulus E_{C}, Poisson's ratio ν_{C}, density ρ_{C} and magnetic permeability η_{C} [18]:

$$E_{\mathrm{C}}=\frac{3}{8}\frac{1+\xi_{\mathrm{L}}\eta_{\mathrm{L}}V_{\mathrm{G}}}{1-\eta_{\mathrm{L}}V_{\mathrm{G}}}\times E_{\mathrm{M}}+\frac{5}{8}\frac{1+\xi_{\mathrm{W}}\eta_{\mathrm{W}}V_{\mathrm{G}}}{1-\eta_{\mathrm{W}}V_{\mathrm{G}}}\times E_{\mathrm{M}} \tag{1a}$$

$$\nu_{\mathrm{C}}=\nu_{\mathrm{G}}V_{\mathrm{G}}+\nu_{\mathrm{M}}\left(1-V_{\mathrm{G}}\right) \tag{1b}$$

$$\rho_{\mathrm{C}}=\rho_{\mathrm{G}}V_{\mathrm{G}}+\rho_{\mathrm{M}}\left(1-V_{\mathrm{G}}\right) \tag{1c}$$

$$\eta_{\mathrm{C}}=\eta_{\mathrm{G}}V_{\mathrm{G}}+\eta_{\mathrm{M}}\left(1-V_{\mathrm{G}}\right) \tag{1d}$$

where

$$\eta_{\mathrm{L}}=\frac{\left(E_{\mathrm{G}}/E_{\mathrm{M}}\right)-1}{\left(E_{\mathrm{G}}/E_{\mathrm{M}}\right)+\xi_{\mathrm{L}}},\ \eta_{\mathrm{W}}=\frac{\left(E_{\mathrm{G}}/E_{\mathrm{M}}\right)-1}{\left(E_{\mathrm{G}}/E_{\mathrm{M}}\right)+\xi_{\mathrm{W}}} \tag{2}$$

in which the subscripts "G" and "M" correspond to GPL and matrix material respectively; V_{G} is GPL volume fraction; $\xi_{\mathrm{L}}=2(l_{\mathrm{G}}/h_{\mathrm{G}})$ and $\xi_{\mathrm{W}}=2(b_{\mathrm{G}}/h_{\mathrm{G}})$ are related to GPL geometry and size, where l_{G}, b_{G} and h_{G} are the average length, width and thickness of GPLs, respectively.

2.1. Rotational spring model

In this paper, the case when the open edge crack perpendicular to the surface of the beam is considered. The massless rotational spring model is used to model the cracked FG-GPLRC beam (see Fig. 1(c)) because its effectiveness and accuracy have been verified [17]. According to the theory of fracture mechanics, the flexibility G caused by the crack is related to the stress intensity factor at the crack tip:

$$\frac{1-\nu(a)^2}{E(a)}K_{\mathrm{I}}^2=\frac{M^2}{2}\frac{\mathrm{d}G}{\mathrm{d}a} \tag{3}$$

in which M is the bending moment of the cross-section of the crack; K_{I} is the stress intensity factor of mode I crack tip under bending load [17]; $E(a)$ and $\nu(a)$ are Young's modulus and Poisson's ratio at the crack tip, respectively. Combining Eq. (3) and the normalized stress intensity factor $F(a)=K_{\mathrm{I}}h^2/(6M\sqrt{\pi a})$ yields

$$G=\frac{72\pi}{h^2}\int_0^{\xi}\frac{1-\nu(\varsigma h)^2}{E(\varsigma h)}\varsigma F^2(\varsigma)\mathrm{d}\varsigma \tag{4}$$

where $\varsigma=a/h$. Then the stiffness of the rotational spring can be obtained via

$$K_{\mathrm{T}}=\frac{1}{G} \tag{5}$$

2.2. Strain energy and potential energy

According to the first-order shear deformation beam theory, the displacements of any point in segment m (m = 1, 2) along the X and Z directions are as follows:

$$\begin{aligned}\bar{U}_m(x,z,t)&=U_m(x,t)+z\psi_m(x,t),\\ \bar{W}_m(x,z,t)&=W_m(x,t)\end{aligned} \tag{6}$$

in which $U_m(x,t)$ and $W_m(x,t)$ are the axial and transverse displacements of a point at the neutral plane, respectively; $\psi_m(x,t)$ is the angular displacement of the cross-section; t is time. The linear strain-displacement relationship is considered:

$$\varepsilon_{xm}=\frac{\partial U_m}{\partial x}+z\frac{\partial \psi_m}{\partial x},\ \ \gamma_{xzm}=\frac{\partial W_m}{\partial x}+\psi_m \tag{7}$$

then the kinetic energy K and potential energy V of the beam can be expressed as:

$$K=\frac{1}{2}\sum_{m=1}^{2}\int_{L_{0m}}^{L_{1m}}\int_{-h/2}^{h/2}\rho_C\left[\left(\frac{\partial\bar{U}_m}{\partial t}\right)^2+\left(\frac{\partial W_m}{\partial t}\right)^2\right]\mathrm{d}z\mathrm{d}x \tag{8a}$$

$$\begin{aligned}V=&\frac{1}{2}\sum_{m=1}^{2}\int_{L_{0m}}^{L_{1m}}\int_{-h/2}^{h/2}\left(Q_{11}\varepsilon_{xm}^2+Q_{55}\gamma_{xzm}^2\right)\mathrm{d}z\mathrm{d}x\\&+\frac{1}{2}K_{\mathrm{T}}\left[\psi_2(L_1)-\psi_1(L_1)\right]^2\end{aligned} \tag{8b}$$

The stiffness components and the inertia-related terms are defined as:

$$\left\{A_{11},B_{11},D_{11}\right\}=\int_{-h/2}^{h/2}Q_{11}\left\{1,z,z^2\right\}\mathrm{d}z \tag{9a}$$

$$A_{55}=\int_{-h/2}^{h/2}\kappa Q_{55}\mathrm{d}z \tag{9b}$$

$$\left\{I_1,I_2,I_3\right\}=\int_{-h/2}^{h/2}\rho_C\left\{1,z,z^2\right\}\mathrm{d}z \tag{9c}$$

where $\kappa = 5/6$ is shear correction factor; $Q_{11} = E_C / (1-\nu_C^2)$; $Q_{55} = E_C / 2(1+\nu_C)$. It is worth noting that both B_{11} and I_2 are zero in the cases of the three GPL distribution patterns considered in this paper due to the symmetry.

2.3. Maxwell's relation

By ignoring the Thompson effect, Maxwell electrodynamic equations in elastic media are [19]:

$$\mathbf{J} = \nabla \times \mathbf{h} \tag{10a}$$

$$\nabla \times \mathbf{e} = -\eta_{\mathrm{C}} \frac{\partial \mathbf{h}}{\partial t} \tag{10b}$$

$$\nabla \cdot \mathbf{h} = 0 \tag{10c}$$

$$\mathbf{e} = -\eta_{\mathrm{C}} \left(\frac{\partial \mathbf{U}}{\partial t} \times \mathbf{H} \right) \tag{10d}$$

where **J** is current density; **h** and **e** are the distribution of the induced magnetic field and the intensity of the induced electric field caused by the motion of the beam, respectively; $\nabla = (\partial / \partial x)\mathbf{i} + (\partial / \partial y)\mathbf{j} + (\partial / \partial z)\mathbf{k}$ is Hamilton operator; $\mathbf{U} = \bar{U}_m \mathbf{i} + 0\ \mathbf{j} + \bar{W}_m \mathbf{k}$ is the displacement field of the beam; **i**, **j** and **k** are unit vectors in *X*, *Y* and *Z* directions, respectively. **H** is the magnetic field distribution in the free space. Substituting Eqs (10d) and (10b) yields

$$\mathbf{h} = \nabla \times (\mathbf{U} \times \mathbf{H}) \tag{11}$$

Considering the axial magnetic field, i.e., $\mathbf{H} = H_x \mathbf{i}$, and substituting Eq. (6) into Eq. (11) yields

$$\mathbf{h} = -H_x \frac{\partial \bar{W}_m}{\partial z} \mathbf{i} + H_x \frac{\partial \bar{W}_m}{\partial x} \mathbf{k} \tag{12}$$

then the Lorentz force generated from the axial magnetic field is:

$$f_m = \eta_{\mathrm{C}} (\mathbf{J} \times \mathbf{H}) = \eta_{\mathrm{C}} H_x^2 \frac{\partial^2 \bar{W}_m}{\partial x^2} \mathbf{k} \tag{13}$$

Ideal graphene is intrinsically non-magnetic and lacks localized magnetic moment due to the delocalized π-bonding network. In this regard, in it is assumed that the permeability η_{G} of GPLs is zero [20] in this work. According to Eqs. (6) and (13), the Lorentz magnetic force are:

$$\begin{aligned} F_{lm} &= \int_{-h/2}^{h/2} f_z dz = H_x^2 \frac{\partial^2 W_m}{\partial x^2} \int_{-h/2}^{h/2} \eta_{\mathrm{C}} dz \\ &= H_x^2 \frac{\partial^2 W_m}{\partial x^2} \int_{-h/2}^{h/2} \eta_{\mathrm{M}} (1 - V_{\mathrm{G}}) dz = \eta_{\mathrm{M}} h \left(1 - V_{\mathrm{G}}^*\right) H_x^2 \frac{\partial^2 W_m}{\partial x^2} \end{aligned} \tag{14}$$

where V_{G}^* is the total GPL volume fraction, which is related to the total GPL weight fraction g_{G}:

$$V_{\mathrm{G}}^{*}=\frac{g_{\mathrm{G}}}{g_{\mathrm{G}}+(\rho_{\mathrm{G}}/\rho_{\mathrm{M}})(1-g_{\mathrm{G}})} \tag{15}$$

The external work done by axial excitation $N_{\mathrm{x}0}$ and magnetic force is

$$\Upsilon_{\mathrm{p}}=\frac{1}{2}\sum_{m=1}^{2}\int_{L_{0m}}^{L_{1m}}\left[N_{\mathrm{x}0}\left(\frac{\partial W_m}{\partial x}\right)^2+F_{lm}W_m\right]\mathrm{d}x \tag{16}$$

3. SOLUTION PROCEDURE

3.1. Ritz trial functions

The convergence of the solution can be promoted by selecting trial functions which satisfy both the geometric boundary conditions at the beam ends and the compatibility conditions between the two beam segments at the cracked cross section. In this case, the trial functions for the beam segments can be set up by following two steps: first, the trial functions for the beam segments that only satisfy their own geometric boundary conditions are set up; then the trial function of segment 1 are modified to guarantee the compatibility conditions. Introducing the following dimensionless quantities:

$$\begin{gathered}\zeta_1=\frac{x}{L},\quad \zeta_2=\frac{x-L_1}{L-L_1},\quad (u,w)=\frac{(U,W)}{h},\varphi=\psi,\\ \alpha=\frac{L_1}{h},\quad \alpha_1=\frac{L-L_1}{h},\quad \tau=t\sqrt{\frac{A_{11}}{I_1L_1(L-L_1)}},\\ \left(\bar{I}_3,d_{11},a_{55}\right)=\left(\frac{I_3}{I_1h^2},\frac{D_{11}}{A_{11}h^2},\frac{A_{55}}{A_{11}}\right),\quad \beta=\frac{L-L_1}{L_1},\\ k_{\mathrm{T}}=\frac{L-L_1}{A_{11}h^2}K_{\mathrm{T}},\quad P=\frac{N_{x0}}{A_{11}},\quad H_x^{*}=\frac{\eta_{\mathrm{M}}hH_x^2}{A_{11}}\end{gathered} \tag{17}$$

then the compatibility conditions of the beam at the cracked section are as follows:

$$\begin{gathered}u_1(1)=u_2(0),\quad w_1(1)=w_2(0),\\ k_T[\varphi_2(0)-\varphi_1(1)]=d_{11}\frac{\partial\varphi_2(0)}{\partial\zeta_2}\end{gathered} \tag{18}$$

The displacements of the clamped-clamped (C-C) beam can be set up as

$$\begin{gathered}u_1=\sum_{j=1}^{N}A_j\zeta_1^j\left(1-\zeta_1\right)+\zeta_1\sum_{j=1}^{N}a_j,\quad u_2=\sum_{j=1}^{N}a_j(1-\zeta_2)^j,\\ w_1=\sum_{j=1}^{N}B_j\zeta_1^j\left(1-\zeta_1\right)+\zeta_1\sum_{j=1}^{N}b_j,\quad w_2=\sum_{j=1}^{N}b_j(1-\zeta_2)^j,\\ \varphi_1=\sum_{j=1}^{N}C_j\zeta_1^j\left(1-\zeta_1\right)+\zeta_1\sum_{j=1}^{N}c_j\left(1+\frac{jd_{11}}{k_{\mathrm{T}}}\right),\quad \varphi_2=\sum_{j=1}^{N}c_j(1-\zeta_2)^j\end{gathered} \tag{19}$$

The angular displacements of the hinged-hinged (H-H) and clamped-hinged (C-H)

beams are different from those of the C-C beams, i.e.,

$$\varphi_1=\sum_{j=1}^{N}C_j\left(1-\zeta_1\right)^j+\zeta_1\sum_{j=1}^{N}c_j\left(1-\frac{jd_{11}}{k_{\mathrm{T}}}\right),\ \varphi_2=\sum_{j=1}^{N}c_j(1+\zeta_2)^j$$

for the H-H beams, and

$$\varphi_1=\sum_{j=1}^{N}C_j\zeta_1^j\left(1-\zeta_1\right)+\zeta_1\sum_{j=1}^{N}c_j\left(1-\frac{jd_{11}}{k_{\mathrm{T}}}\right),\quad \varphi_2=\sum_{j=1}^{N}c_j(1+\zeta_2)^j \tag{21}$$

for the C-H beams.

3.2. Dynamic stability analysis

Substituting Eqs. (8) and (16) into the second kind of Lagrange equation:

$$\frac{\mathrm{d}}{\mathrm{d}\tau}\left(\frac{\partial\Pi}{\partial\dot{d}_l}\right)-\frac{\partial\Pi}{\partial d_l}=Q_l,\quad l=1,2,...,6N \tag{22}$$

where $\Pi=K-V$, $Q_l=\partial\Upsilon_{\mathrm{p}}/\partial d_l$, and d_l stands for unknown coefficient A_j, B_j, C_j, a_j, b_j or c_j. Furthermore, considering Eq. (17), the dimensionless motion equation of the cracked beam can be obtained:

$$\mathbf{M}\ddot{\mathbf{d}}+\left(\mathbf{K}_{\mathrm{L}}-\mathbf{K}_{\mathrm{H}}-P\,\mathbf{K}_{\mathrm{P}}\right)\mathbf{d}=\mathbf{0} \tag{23}$$

where $\mathbf{d}=\left\{\{A_j\}^{\mathrm{T}}\{a_j\}^{\mathrm{T}}\{B_j\}^{\mathrm{T}}\{b_j\}^{\mathrm{T}}\{C_j\}^{\mathrm{T}}\{c_j\}^{\mathrm{T}}\right\}^{\mathrm{T}}$, $\mathbf{M}$ is the mass matrix, $\mathbf{K}_{\mathrm{L}}$ is the stiffness matrix, $\mathbf{K}_{\mathrm{H}}$ and $\mathbf{K}_{\mathrm{P}}$ are the geometric stiffness matrix. This paper considers the case of axial periodic load, i.e.,

$$P=P_{\mathrm{s}}+P_{\mathrm{d}}\cos\theta\tau \tag{24}$$

where P_{s} and P_{d} represent static and dynamic load components, respectively.

Expanding the displacement vector **d** in the following series:

$$\mathbf{d}=\sum_{\mathrm{n}=1,3,\ldots}^{\infty}\boldsymbol{\alpha}_{\mathrm{n}}\sin\left(\frac{n\theta\tau}{2}\right)+\boldsymbol{\beta}_{\mathrm{n}}\cos\left(\frac{n\theta\tau}{2}\right) \tag{25}$$

where $\boldsymbol{\alpha}_{\mathrm{n}}$ and $\boldsymbol{\beta}_{\mathrm{n}}$ are arbitrary constant vectors. The Bolotin method [21] shows that the first-order approximation of Eq. (23) can provide good accuracy for calculating the boundary of the unstable region. Substituting Eqs. (22) and (23) into Eq. (21), two independent eigenvalue equations are obtained:

$$\left[\mathbf{K}_{\mathrm{L}}-\mathbf{K}_{\mathrm{H}}-\left(P_{\mathrm{s}}-\frac{P_{\mathrm{d}}}{2}\right)\mathbf{K}_{\mathrm{P}}-\frac{\theta^2}{4}\mathbf{M}\right]\boldsymbol{\alpha}_1=0 \tag{26a}$$

$$\left[\mathbf{K}_{\mathrm{L}}-\mathbf{K}_{\mathrm{H}}-\left(P_{\mathrm{s}}+\frac{P_{\mathrm{d}}}{2}\right)\mathbf{K}_{\mathrm{P}}-\frac{\theta^2}{4}\mathbf{M}\right]\boldsymbol{\beta}_1=0 \tag{26b}$$

Two critical excitation frequencies θ can be obtained as two eigenvalues of Eqs. (26a) and (26b) for a given value of P_{d}. The principle unstable region can then

be determined which is surrounded by the two lines of θ vs P_d.

4. NUMERICAL RESULTS AND DISCUSSION

4.1. Comparison studies

In this section, through an example, the present results are compared with those in the open literature to verify the accuracy of the present method. Tables 1 and 2 show the dimensionless fundamental frequencies and critical buckling loads of cracked functionally graded material (FGM) beams clamped at both ends without magnetic field, respectively. Beam thickness h = 0.1 m and crack depth ratio is 0.2. Young's modulus and the density of the beams follow the variation law of exponential function along the thickness direction, that is, $E(Z)=E_0\exp(\beta Z)$, $\rho(Z)=\rho_0\exp(\beta Z)$. Poisson's ratio remains constant 0.33. The elastic modulus and density of the material on the top surface of the beams are $E_1=70\,\text{GPa}$ and $\rho_1=2780\,\text{kg/m}^3$, respectively. Table 1 shows the results for the case when the crack is located at the midspan of the beam. Table 2 shows the results for the case when Young's modulus ratio $E_2/E_1=5$, in which E_2 is Young's modulus of the material on the bottom surface and the slenderness ratio of the beam is 6. It is observed that the errors between the present results and those in Ref. [22] are tiny.

Table 1 Dimensionless fundamental frequencies of cracked FGM beams.

E_2/E_1	L/h=6			L/h=16		
	Present	Ref. [22]	Error	Present	Ref. [22]	Error
0.2	0.8197	0.8125	0.89%	0.3600	0.3602	0.04%
1.0	0.8688	0.8584	1.21%	0.3848	0.3840	0.20%
5.0	0.8416	0.8289	1.52%	0.3653	0.3641	0.33%

Table 2 Dimensionless critical buckling loads of cracked FGM beams.

	L_1/L						
	0.1	0.2	0.3	0.4	0.5	0.6	0.7
Ref [22]	0.1487	0.1544	0.1552	0.1510	0.1484	0.1510	0.155 2
Present	0.1494	0.1544	0.1544	0.1487	0.1457	0.1487	0.1544
Error	0.47%	0.00%	0.52%	1.52%	1.82%	1.52%	0.52%

4.2. Parametric studies

In the following numerical simulation, the length and thickness of the cracked GPLs/epoxy beams with 10 stacked layers are selected as 1.2m and 0.12m, respectively. Unless otherwise specified, the cracked beams are clamped at both ends. The average dimensions of GPLs are $l_G=2.5\,\mu\text{m}$, $w_G=1.5\,\mu\text{m}$ and $h_G=1.5\,\text{nm}$, respectively. The material parameters of two components can be found in Ref. [17].

Fig. 2 studies the influence of GPL distribution pattern on the linear

principle unstable regions of the cracked beams under magnetic field. It is observed that with the same crack depth and location, the FG-X beams have the highest resonance frequencies, and the FG-O beams have the lowest ones. Compared with the UD beam, the principle unstable region of the FG-X beam is further away from the coordinate origin, and that of the FG-O beam is nearer to the coordinate origin. This illustrates that the distribution of GPLs further away from the neutral layer has a better strengthening effect on the structure. It is also observed that the enhancement of the magnetic field has a significant effect on improving the dynamic stability of the beams. The change of magnetic field has the greatest effect on the principle unstable regions of the FG-O beams and the least effect on those of the FG-X beams.

Fig. 3 displays the influence of boundary conditions on the linear principle unstable regions of the cracked FG-X beams under magnetic field with different intensities. It is found that the C-C beams have the best stability behavior. In addition, the principle unstable regions of the H-H (C-C) beams are most (least) affected by the enhancement of magnetic field.

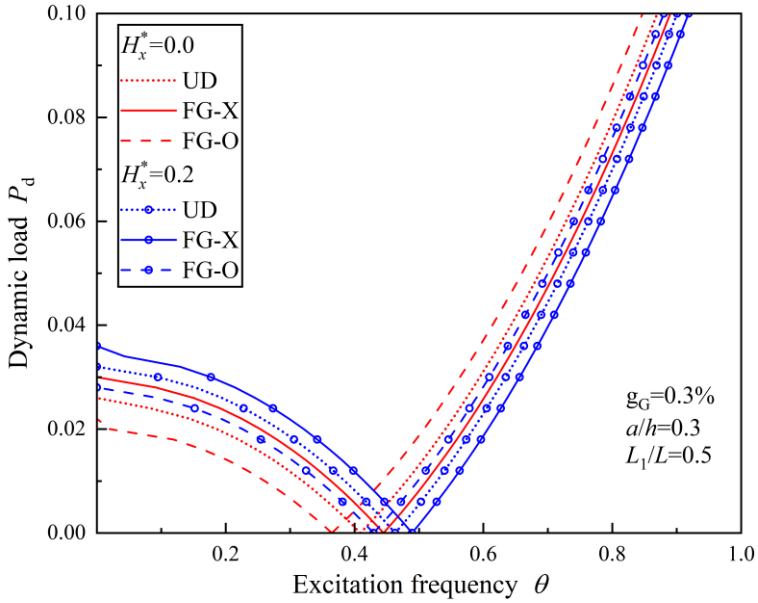

Fig. 2. Influence of GPL distribution pattern on the linear principle unstable regions of the beams under magnetic field

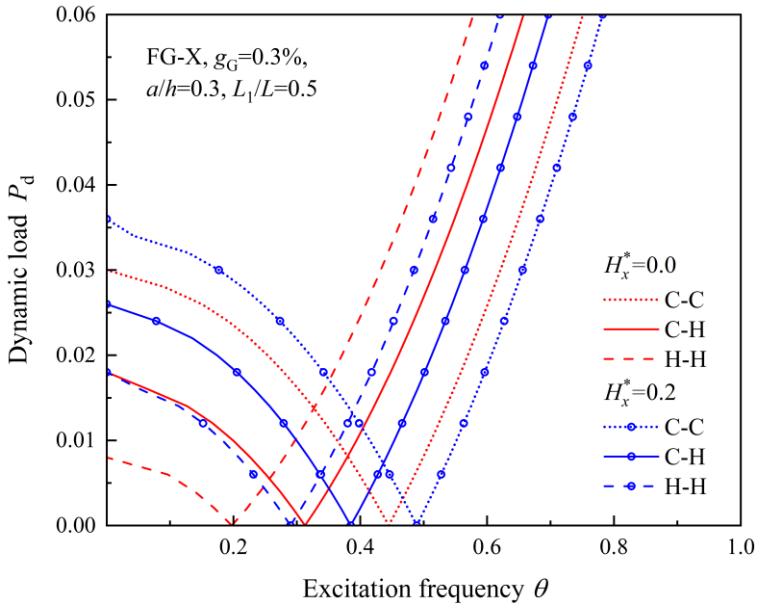

Fig. 3. Influence of boundary conditions on the linear principle unstable regions of the beams under magnetic field

Fig. 4 investigates the influence of crack depth on the linear principle unstable regions of the FG-X beam under magnetic field. Four cases are considered, in which the crack depth ratios are selected as 0.0, 0.1, 0.2 and 0.3, respectively. Note that the crack depth ratio of 0.0 means that the beam is intact. It is observed that with the increase of the crack depth, the principle unstable region moves to the coordinate origin, and the width of the principle unstable region increases. This illustrates that the increase of crack depth reduces the stability of the beam. It can be further observed that the width of the principle unstable region increases faster and faster with the increase of crack depth.

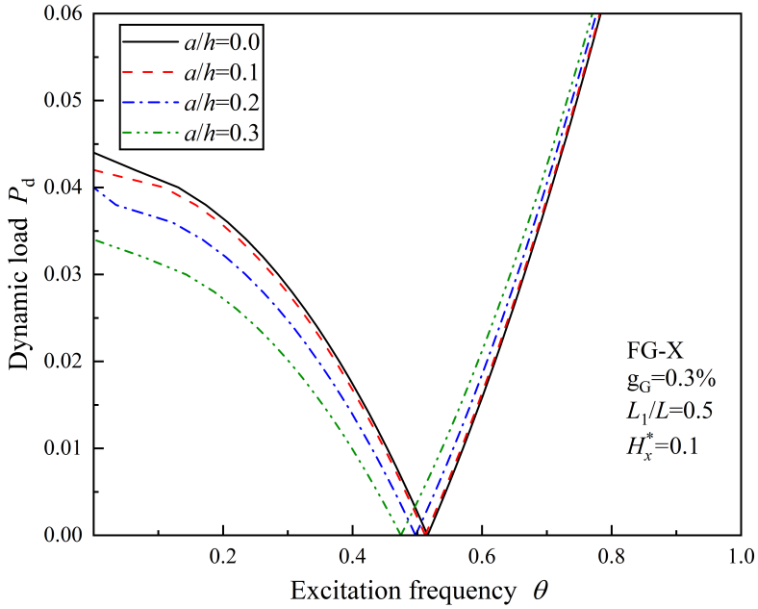

Fig. 4. Influence of crack depth on the linear principle unstable regions of the beams under magnetic field

Fig. 5 illustrates the influence of crack location on the linear principle unstable regions of the beam under magnetic field. As the crack location moves from the end support to the midspan, both the width of the linear principle unstable region and the resonance frequency increase. Further observation shows that the change of crack location has a much more influence on the resonance frequency when the crack is near the support ends than when it is near the midspan.

Fig. 6 presents the influence of magnetic field intensity on the linear principle unstable regions of the FG-X beam. It is observed that during the process of increasing the intensity of the magnetic field, the principle unstable region of the beam first moves to higher excitation frequency, and then moves to lower excitation frequency when H_x^* reaches about 0.3. This is because the magnetic field force not only reduces the stability but also improves the bending stiffness of the beam since it is in the transverse direction of the beam, and its magnitude is related to the transverse displacement of the beam. The influence of increasing stiffness is greater than that of reducing stability when the magnetic field is weak, while it is a different scenario when the magnetic field is strong.

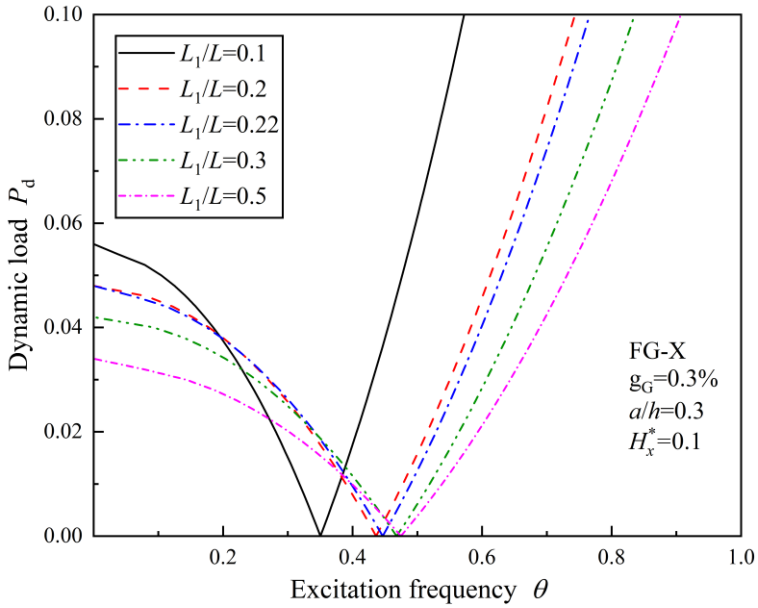

Fig. 5. Influence of crack location on the linear principle unstable regions of the beams under magnetic field

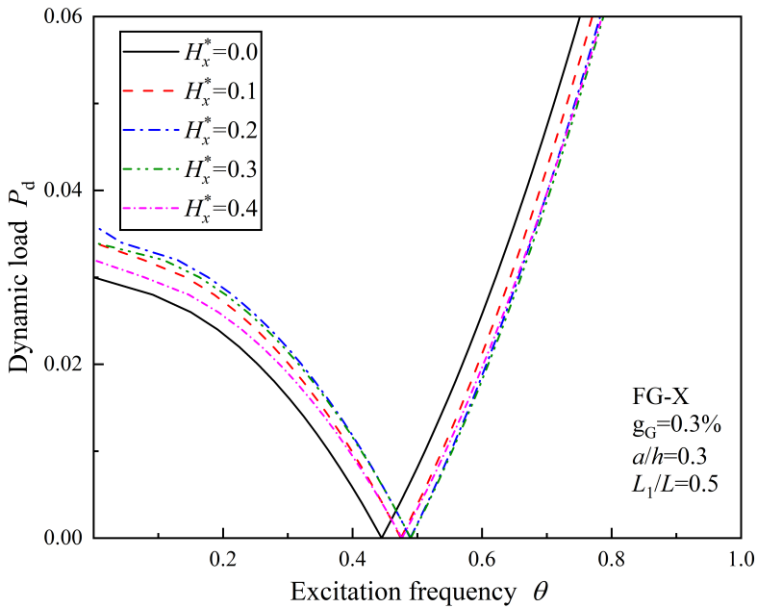

Fig. 6. Influence of magnetic field intensity on the linear principle unstable regions of the beams

5. CONCLUSIONS

In this paper, the linear dynamic stability of cracked FG-GPLRC beams under the coupling action of axial load and magnetic field is studied. The mechanical parameters of GPL-reinforced composites are estimated by micromechanical model and mixing rule. The governing equations of cracked beam are derived by combining Ritz method with Lagrange equation. Bolotin method is used to determine the principle unstable regions. The numerical results show that: (1) The dynamic stability of cracked beams can be improved by properly strengthening the magnetic field. However, a too strong magnetic field may reduce the dynamic stability of the beam. (2) The FG-X beam with clamped-clamped boundaries has the best dynamic stability and is least sensitive to the variation of the magnetic field. On the contrary, the FG-O beam with hinged-hinged boundaries has the worst dynamic stability and is most sensitive to the variation of the magnetic field. (3) The presence of crack reduces the resonance frequencies of the beams and increases the sizes of the linear principle unstable regions, and this effect varies with the crack position.

ACKNOWLEDGEMENTS

This work is supported by the Natural Science Foundation of Jiangsu Province (Grant Nos. BK20201414).

REFERENCES

[1] Qin Z, Wu YT, Eizad A, Lyu SK, Lee CM. Advancement of Mechanical Engineering in Extreme Environments. International Journal of Precision

Engineering and Manufacturing-Green Technology. 2021;8(6):1767-82.
[2] Rafiee MA, Rafiee J, Wang Z, Song HH, Yu ZZ, Koratkar N. Enhanced Mechanical Properties of Nanocomposites at Low Graphene Content. Acs Nano. 2009;3(12):3884-90.
[3] Mortazavi B, Benzerara O, Meyer H, Bardon J, Ahzi S. Combined molecular dynamics-finite element multiscale modeling of thermal conduction in graphene epoxy nanocomposites. Carbon. 2013;60:356-65.
[4] Wang Y, Yu JH, Dai W, Song YZ, Wang D, Zeng LM, et al. Enhanced Thermal and Electrical Properties of Epoxy Composites Reinforced With Graphene Nanoplatelets. Polymer Composites. 2015;36(3):556-65.
[5] Song MT, Kitipornchai S, Yang J. Free and forced vibrations of functionally graded polymer composite plates reinforced with graphene nanoplatelets. Composite Structures. 2017;159:579-88.
[6] Yang J, Wu HL, Kitipornchai S. Buckling and postbuckling of functionally graded multilayer graphene platelet-reinforced composite beams. Composite Structures. 2017;161:111-8.
[7] Chen D, Yang J, Kitipornchai S. Nonlinear vibration and postbuckling of functionally graded graphene reinforced porous nanocomposite beams. Composites Science and Technology. 2017;142:235-45.
[8] Kitipornchai S, Chen D, Yang J. Free vibration and elastic buckling of functionally graded porous beams reinforced by graphene platelets. Materials & Design. 2017;116:656-65.
[9] Li KY, Wu D, Chen XJ, Cheng J, Liu ZY, Gao W, et al. Isogeometric Analysis of functionally graded porous plates reinforced by graphene platelets. Composite Structures. 2018;204:114-30.
[10] Lei ZX, Su QQ, Zeng HP, Zhang Y, Yu CH. Parametric studies on buckling behavior of functionally graded graphene-reinforced composites laminated plates in thermal environment. Composite Structures. 2018;202:695-709.
[11] Ke LL, Yang J, Kitipornchai S. Dynamic Stability of Functionally Graded Carbon Nanotube-Reinforced Composite Beams. Mechanics of Advanced Materials and Structures. 2013;20(1):28-37.
[12] Wu HL, Yang J, Kitipornchai S. Dynamic instability of functionally graded multilayer graphene nanocomposite beams in thermal environment. Composite Structures. 2017;162:244-54.
[13] Zhao SY, Yang ZC, Kitipornchai S, Yang J. Dynamic instability of functionally graded porous arches reinforced by graphene platelets. Thin-Walled Structures. 2020;147:106491.
[14] Yang ZC, Liu AR, Yang J, Fu JY, Yang B. Dynamic buckling of functionally graded graphene nanoplatelets reinforced composite shallow arches under a step central point load. Journal of Sound and Vibration. 2020;465:115019.
[15] Sobhy M. Buckling and vibration of FG graphene platelets/aluminum sandwich curved nanobeams considering the thickness stretching effect and

exposed to a magnetic field. Results in Physics. 2020;16:102865.
[16] Zhang CW, Wang LM, Eyvazian A, Khan A, Sebaey TA. Analytical solution for static and dynamic analysis of FGP cylinders integrated with FG-GPLs patches exposed to longitudinal magnetic field. Engineering with Computers. (*in press*).
[17] Song MT, Gong YH, Yang J, Zhu WD, Kitipornchai S. Free vibration and buckling analyses of edge-cracked functionally graded multilayer graphene nanoplatelet-reinforced composite beams resting on an elastic foundation. Journal of Sound and Vibration. 2019;458:89-108.
[18] Liu DY. Free Vibration of Functionally Graded Graphene Platelets Reinforced Magnetic Nanocomposite Beams Resting on Elastic Foundation. Nanomaterials. 2020;10(11):2193.
[19] Rad AB, Shariyat M. Three-dimensional magneto-elastic analysis of asymmetric variable thickness porous FGM circular plates with non-uniform tractions and Kerr elastic foundations. Composite Structures. 2015;125:558-74.
[20] Orlita M, Escoffier W, Plochocka P, Raquet B, Zeitler U. Graphene in high magnetic fields. Comptes Rendus Physique. 2013;14(1):78-93.
[21] Bolotin VVe. The Dynamic Stability of Elastic Systems. American Journal of Physics. 1965;33(9):752-3.
[22] Ke LL, Yang J, Kitipornchai S, Xiang Y. Flexural Vibration and Elastic Buckling of a Cracked Timoshenko Beam Made of Functionally Graded Materials. Mechanics of Advanced Materials and Structures. 2009;16(6):488-502.